



Oxidation dynamics of aluminum nanorods

Ying Li, Rajiv K. Kalia, Aiichiro Nakano, and Priya Vashishta

Citation: [Applied Physics Letters](#) **106**, 083101 (2015); doi: 10.1063/1.4913490

View online: <http://dx.doi.org/10.1063/1.4913490>

View Table of Contents: <http://scitation.aip.org/content/aip/journal/apl/106/8?ver=pdfcov>

Published by the [AIP Publishing](#)

A banner for Applied Physics Letters featuring the journal's logo and the text 'Meet The New Deputy Editors'. Below the text are three circular portraits of the new deputy editors: Alexander A. Balandin, Qing Hu, and David L. Price.

AIP | Applied Physics Letters

Meet The New Deputy Editors

 Alexander A. Balandin

 Qing Hu

 David L. Price

Oxidation dynamics of aluminum nanorods

Ying Li,¹ Rajiv K. Kalia,² Aiichiro Nakano,² and Priya Vashishta²

¹Argonne Leadership Computing Facility, Argonne National Laboratory, Argonne, Illinois 60439, USA

²Collaboratory for Advanced Computing and Simulations, Department of Physics and Astronomy, Department of Chemical Engineering and Materials Science, Department of Computer Science, University of Southern California, Los Angeles, California 90089-0242, USA

(Received 30 December 2014; accepted 11 February 2015; published online 23 February 2015)

Aluminum nanorods (Al-NRs) are promising fuels for pyrotechnics due to the high contact areas with oxidizers, but their oxidation mechanisms are largely unknown. Here, reactive molecular dynamics simulations are performed to study thermally initiated burning of oxide-coated Al-NRs with different diameters ($D = 26, 36,$ and 46 nm) in oxygen environment. We found that thinner Al-NRs burn faster due to the larger surface-to-volume ratio. The reaction initiates with the dissolution of the alumina shell into the molten Al core to generate heat. This is followed by the incorporation of environmental oxygen atoms into the resulting Al-rich shell, thereby accelerating the heat release. These results reveal an unexpectedly active role of the alumina shell as a “nanoreactor” for oxidation. © 2015 AIP Publishing LLC. [<http://dx.doi.org/10.1063/1.4913490>]

Aluminum (Al) nanoparticles are widely used for propellants and explosives because of their high volumetric energy density,¹ high heat-release rate,² low ignition temperature,³ and rapid heat propagation.⁴ During combustion, Al nanoparticles tend to melt and coalesce into large agglomerates,^{5,6} which makes the combustion behavior highly complex.^{7,8} For example, slow burning of these agglomerates prevent continuous combustion.⁹ The agglomeration also results in uneven size and composition distributions of the mixed fuel and oxidizer particles. This is detrimental to the performance through, e.g., incomplete Al combustion,¹⁰ instabilities,¹¹ and slag formation.¹² In order to overcome these problems, there is a critical need for a new morphology of Al powders.

Various nanomaterial architectures have been explored to achieve this goal by enhancing the homogeneous distribution of oxidizer and fuel.^{13,14} For example, mesoporous structures^{15,16} and nanorods based on self-assembly approaches^{17,18} were used instead of spherical oxidizers to achieve higher contact areas with fuel nanoparticles around them and lower resistance for overall diffusional processes. Alternatively, the same goal may be reached using non-spherical nanofuels. In particular, various methods have recently been developed to synthesize Al nanorods (Al-NRs) and Al nanodisks, including electrodeposition,^{19–21} vapor deposition,²² electromigration,^{23,24} and colloidal lithography.²⁵ For designing Al-NR based energetic composites, it is essential to understand the oxidation dynamics of Al-NRs. A key question is: What is the size effect on the burning speed? Since a native oxide shell exists in all Al-NRs synthesized by the above-mentioned methods, another important question is: What is the role of the oxide shell in the oxidation dynamics?

To answer these questions, we have performed reactive molecular dynamics (RMD) simulations²⁶ of three oxide-coated Al-NRs with diameters $D = 26, 36,$ and 46 nm. Each cylindrical Al-NR has a length of $3D$ and consists of a cylindrical Al core of diameter D' ($=D - 6$ nm) covered by a 3 nm amorphous alumina (Al_2O_3) shell (see Fig. 1). Our Al-

NR simulations with very high surface areas correspond to cases where high heterogeneous surface reaction (HSR) rates play an essential role.²⁷

The oxidation dynamics is studied by heating the left one-third of the Al-NR to a temperature of 1100 K within 9 ps, while the atomic positions of the rest of the Al-NR and the environmental oxygen are fixed at those in the 300 K simulation. The radial distribution function shows that the Al core in the heated left end is liquid at 1100 K. Subsequently, the constraints are removed and the system undergoes oxidation dynamics in the microcanonical ensemble for 1 ns.

Figure 2 shows middle- xz slice snapshots of the $D = 26$ ((a)–(c)), 36 ((d)–(f)), and 46 nm ((g)–(i)) systems at times $t = 1$ ps, 500 ps, and 1 ns. Initial heating of the left one-third of the Al-NR causes slight volume expansion of the left end as shown in Figs. 2(a), 2(d), and 2(g) for $D = 26, 36,$ and 46 nm, respectively. Subsequently, the oxidation front propagates from left to right along the nanorod. At the same time, each Al-NR shortens and its left end deforms into an ellipsoid as shown in Figs. 2(b), 2(e), and 2(h) for $D = 26, 36,$ and 46 nm, respectively. By 1 ns, the entire 26 nm rod has become an ellipsoidal aggregate (Fig. 2(c)), and the majority

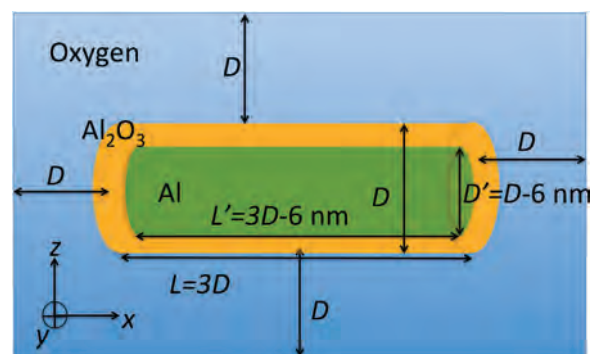


FIG. 1. Schematic of an Al-NR with diameter D and length $L = 3D$. The Al core (shown in green) is covered with a 3 nm-thick alumina shell (orange) and is embedded in oxygen environment (blue).

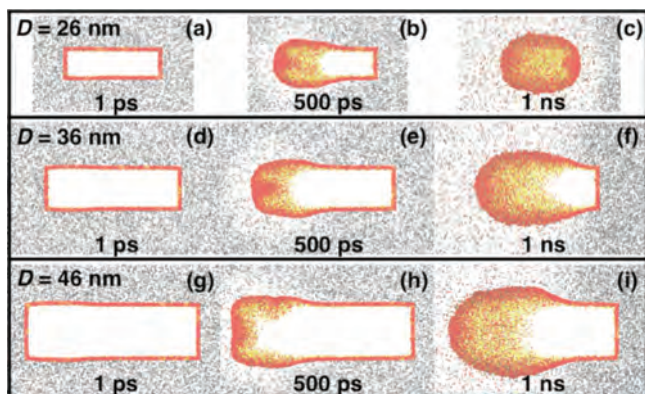


FIG. 2. Middle- xz slice snapshots of $D = 26$, 36, and 46 nm Al-NR systems at times 1 ps, 500 ps, and 1 ns. Only shown are Al atoms from the shell (red dots), O atoms from the shell (yellow dots), and environmental O atoms (black dots).

of the 36 nm rod except its right end has become an ellipsoidal aggregate (Fig. 2(f)). In contrast, only half of the 46 nm rod aggregates as shown in Fig. 2(i). This indicates complete burning of $D = 26$ nm Al-NR by the end of the simulation, while $D = 36$ and 46 nm Al-NRs remain incompletely burned.

To quantify the size dependence of the reactivity, Fig. 3(a) plots the temperature as a function of time for $D = 26$, 36, and 46 nm systems. For all Al-NRs, the temperature increases monotonically as soon as the oxidation reaction starts. Also we note that the temperature is always higher for thinner Al-NRs. To study heat release in the three systems, Fig. 3(b) plots the rate of temperature increase dT/dt as a function of time. While $dT/dt > 0$ at all times in all three systems, the dT/dt exhibits a valley, corresponding to the lowest heat release, at $t = 100$ ps for all Al-NRs. The minimum dT/dt values are different for different diameters, with $D = 26$ nm Al-NR having the highest value. After passing the valley, the rates start to increase, signifying the accelerated heat release. The dT/dt value is always larger, corresponding to faster heat release, for smaller Al-NRs. The decrease of dT/dt for $D = 26$ nm Al-NR after 800 ps is due to the completion of burning. To confirm this interpretation, Fig. 3(c) shows the time evolution of the fraction of unreacted core Al atoms. In fact, the unreacted core Al fraction becomes 0 after 800 ps, indicating complete burning. Fig. 3(d) plots the pressure as a function of time for $D = 26$, 36, and 46 nm systems. The pressure increases monotonically with as the temperature increases. Similar size dependence was also observed for the burning of spherical Al nanoparticles.³¹

In order to understand the cause of the crossover from deceleration to acceleration of heat release in Fig. 3(b), Fig. 4 shows part of the middle xz cross section of the oxide shell in $D = 36$ nm Al-NR before (a) and after (b) the crossover. Here, the oxide shell is identified as the largest fragment interconnected by Al-O bonds, which may contains some of the Al (red) and O (yellow) atoms from the original shell, Al atoms from the original Al core (blue), and environmental O atoms (black). In the early stage, some O atoms from the shell start to react with core Al atoms (see Fig. 4(a) at 50 ps). Namely, we observe reduction of the amorphous

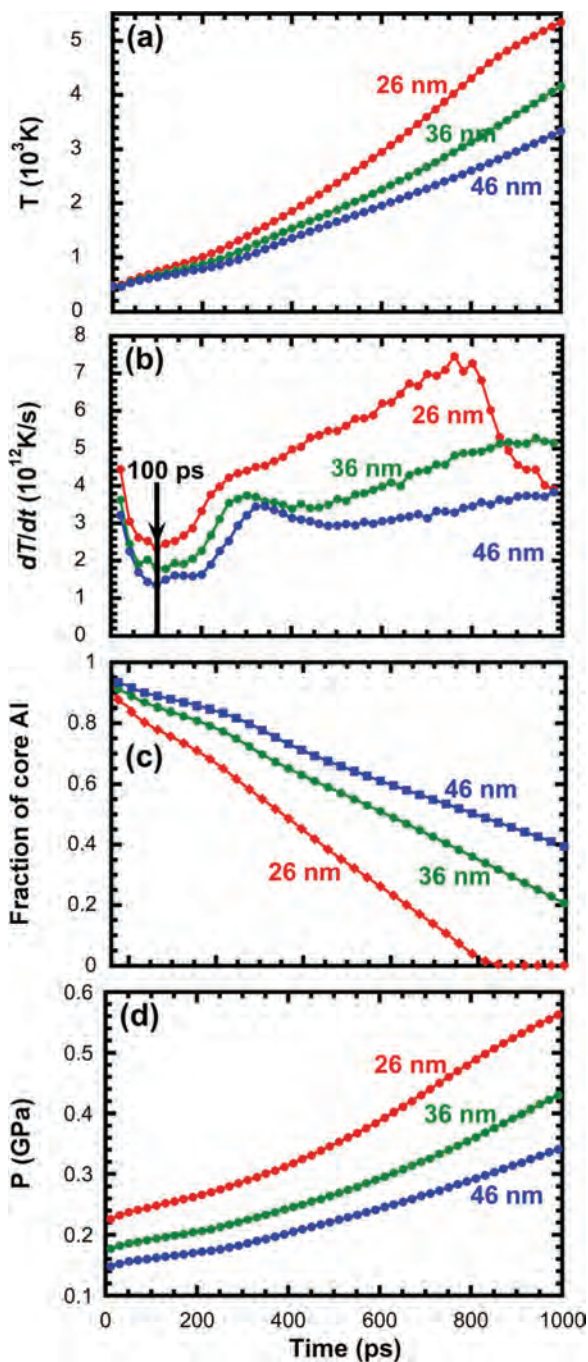


FIG. 3. (a) Temperatures of the three Al-NRs as a function of time. (b) The rates of temperature increase dT/dt of the three Al-NRs as a function of time. (c) The fraction of remaining core Al atoms as a function of time. (d) Pressures of the three Al-NRs as a function of time.

alumina shell involving reactions between liquid Al(l) and solid Al_2O_3 (s) at the core-shell interface. This energy release by interfacial mixing of Al core and Al_2O_3 is akin to the formation of an interphase “complexion” in a solid-solid interface.²⁸ In order to reduce the high energy associated with a sharp interface, a thermodynamically stable interphase of thickness ~ 1 nm is formed, which has distinct atomistic structures that do not exist in bulk. *Ab initio* quantum molecular dynamics simulation showed that melting of one side of the interface significantly accelerates the formation of the interphase,²⁹ which is the case here. A similar

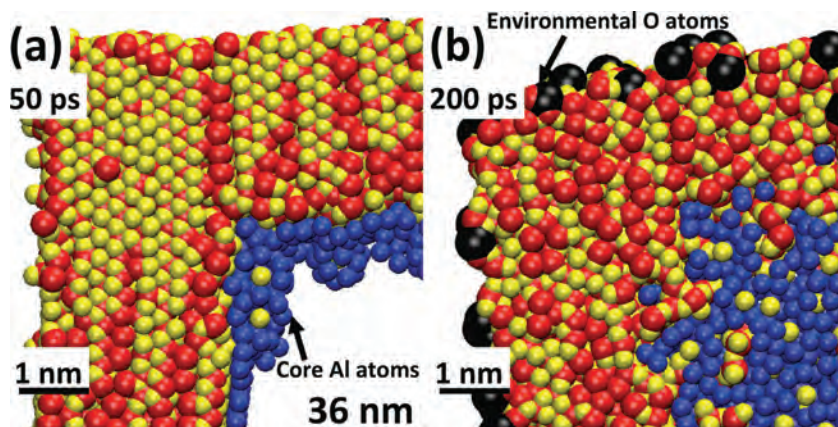


FIG. 4. Snapshots of part of the middle xz slice of the 36 nm system, showing the largest oxide fragment at (a) 50 ps and (b) 200 ps. Original shell Al, shell O, core Al, and environmental O atoms are shown in red, yellow, blue, and black colors, respectively.

high-temperature reduction of alumina at $\text{Al}_2\text{O}_3(\text{s})$ -Al(l) interfaces was observed by Oh *et al.* using high-resolution transmission electron microscopy during vapor-liquid-solid growth of alumina nanowires.³⁰ Subsequently, environmental O atoms get adsorbed onto the outer surface of the shell, while more reactions occur at the core-shell interface due to the oxygen deficiency of the shell (see Fig. 4(b) at 200 ps). Namely, the reduced amorphous shell re-oxidizes, involving reactions between gas-phase $\text{O}(\text{g})$ and $\text{Al}_2\text{O}_3(\text{s})$. These results indicate an unexpected role of the oxide shell as a reactive medium (or nanoreactor). Rather than being an inert separator between the inner Al fuel and outside oxidizer, the oxide shell continuously exchanges its constituent atoms with core Al and environmental O atoms, thus promoting interfacial reactions and heat release. An essential role of oxide layers to support HSR by transporting reactants has been discussed in Ref. 27.

To study the dynamics of the oxide-shell growth, Fig. S1 plots the time evolution of the composition of its constituent atoms from different sources, i.e., the numbers of Al and O atoms from the original shell, original core Al atoms, and original environmental O atoms.²⁶ For all three Al-NRs, core Al atoms are continuously incorporated into the oxide shell, while some of the O atoms are dissolved into the Al core, starting immediately at time 0. The rapid initiation of the core-shell reaction is likely due to the high pressure and temperature of the liquefied Al core. This is similar to the suboxide formation mechanism at alumina-liquid Al interfaces suggested by Laurent *et al.*³¹ On the other hand, environmental O atoms only appear after 200 ps in the oxide shell. This onset time roughly corresponds to the accelerated heat release in Fig. 3(b). We thus attribute the accelerated heat release after 200 ps to the onset of $\text{O}(\text{g})$ - $\text{Al}_2\text{O}_3(\text{s})$ reactions.

To study the stoichiometry of the oxidation product, Fig. 5(a) plots the ratio of the number of O atoms to that of Al atoms in the oxide shell as a function of time for the three Al-NRs. The time evolution of the stoichiometry in $D = 26$ nm Al-NR directly reflects the different stages of the oxidation mentioned above, i.e., reduction of the alumina shell at the core-shell interface, followed by re-oxidization of the Al-rich shell at the environment-shell interface. In this system, the complete consumption of core Al at 800 ps (see Fig. 3(c)) leads to the diminishing partial pressure of Al, and the rest of reactions is between the hot Al-rich aggregate (Fig. 1(c)) and environmental oxygen. For the larger ($D = 36$

and 46 nm) Al-NRs, the second reaction stage is not reached before 1 ns (Fig. 5(a)) due to the slower reaction speeds (Fig. 3(a)). This confirms the active role of the oxide shell as a nanoreactor, instead of an inert dead weight.

Next, we study the spatial propagation of the oxidation reaction along the Al-NR. To do so, Fig. S2(a) shows snapshots of the largest oxide fragment in $D = 36$ nm Al-NR at different times.²⁶ The positions of the oxidation front (red arrows) at different times show that the oxidation reaction propagates from left to right along the Al-NR axis. Figure S2(b) shows the temperature distribution in the same Al-NR. The hot spots shown in red color are located on the outer left surface of the shell.²⁶ Oxidation reaction on the shell generates heat, which promotes further reactions and pushes the oxidation front rightward along the Al-NR axis. The molten Al core has high local pressure. Figure S2(c) shows the pressure distribution in the same Al-NR, where highest pressure is observed in the Al core.

In order to quantify the size effect on the combustion speed, we calculate the oxidation front position as the average position of the rightmost 100 core Al atoms in the largest oxide fragment, as well as the melting front position in core Al as the rightmost position where the temperature of the un-reacted core reaches the melting point, 933.52 K. Figures 5(b)–5(d) shows the oxidation and melting fronts as a function of time for $D =$ (b) 26, (c) 36, and (d) 46 nm Al-NRs, respectively. Linear regression yields the average oxidation-front speed in $D = 26, 36,$ and 46 nm Al-NRs to be $v_o = 88, 70,$ and 60 m/s, respectively. In comparison, the average melting front in core Al propagates at $v_m = 91$ m/s, 72 m/s, and 66 m/s for $D = 26, 36,$ and 46 nm Al-NRs, respectively. The average v_m is larger than v_o in all systems, which signifies that the former dictates the burning of Al-NRs. The faster v_o 's of the smaller Al-NRs are likely caused by the larger surface-to-volume ratios. This is understandable in the light of the active roles of the core-shell and environment-shell interfaces as reaction spots and heat sources to support continuous melting of the metallic core Al. Here, we should note that both the melting and oxidation fronts in $D = 26$ nm Al-NR reach the right end before 1 ns, with the former reaching earlier than the latter (Fig. 5(b)). In $D = 46$ nm Al-NR, v_o is slower than v_m in the first 600 ps, exceeds the latter around 600 ps, and then slows down below v_m toward 1 ns. This can be understood as a result of oxidation in the radial (in addition to axial) direction that contributes significantly in larger Al-NRs. In $D = 46$ nm

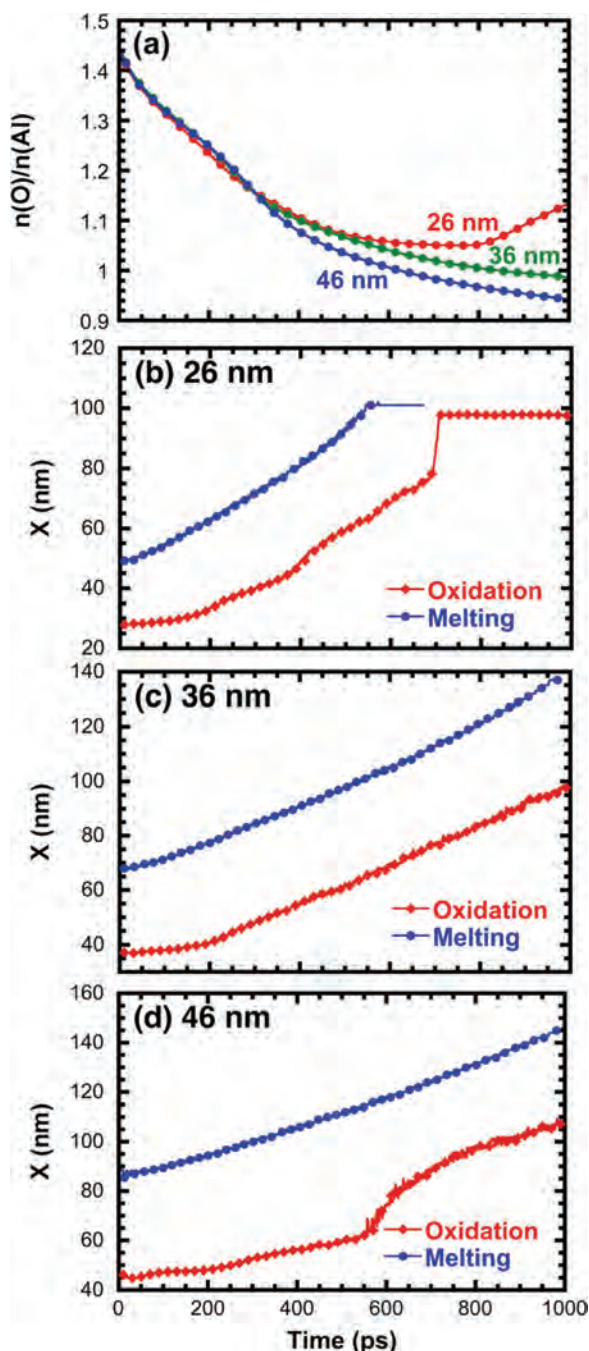


FIG. 5. (a) The ratio of the number of O atoms to that of Al atoms in the oxide shell as a function of time for $D = 26, 36,$ and 46 nm Al-NRs. (b)–(d) Oxidation-front (red) and melting-front (blue) positions as a function of time for $D =$ (b) 26, (c) 36, and (d) 46 nm Al-NRs.

Al-NR, the axial and radial oxidation fronts merge abruptly around 600 ps to cause a sudden advance of the oxidation front.

For a closer look at the heat propagation in Al-NRs, Fig. S5 shows the radial temperature distribution at yz cross-sections in the left one-third, middle one-third, and right one-third parts of $D = 36$ nm Al-NR at different times. We see that the hottest area always is the shell region. This establishes the role of the shell as a heat source to sustain the oxidation reaction.

In summary, RMD simulations of oxide-coated Al-NRs with different diameters reveal the atomistic mechanisms behind the faster oxidation reactions of the smaller Al-NRs.

When one end of an Al-NR is heated to 1100 K and the rest of the nanorod is kept at 300 K in oxygen environment, the nanorod burns from the heated end to the other end along the nanorod axis. The reaction initiates at the interface between the alumina shell and Al core, where shell O atoms react with core Al at high temperature to form bonded interfaces. Subsequently, the fuel-rich oxide shell starts absorbing environmental oxygen for further oxidation. This in turn accelerates the heat release. The smaller nanorods have the faster oxidation-front speeds. The fastest oxidation-front speed in our simulations is 88 m/s for $D = 26$ nm Al-NR. In front of the oxidation, the Al core melts with heat provided by the oxidation reaction. The melting speed has been found to be faster than the oxidation speed for every studied nanorod. For $D = 26$ nm Al-NR, for instance, the melting-front speed is 91 m/s. The faster oxidation-front and melting-front speeds are due to the larger surface-to-volume ratios. Namely, heat produced from the shell interfaces promotes the melting and oxidation of the core Al volume. Thus, enlarging the surface-to-volume ratio is critical for enhancing the burning efficiency. These findings might help understand the combustion behaviors of energetic compounds containing Al-NRs. Future studies may include the effects of different environment and other elements such as dopants and plasticizers, and the interaction of shock waves with these oxidation reactions.

This research work was started with support from the Basic Research Program of Defense Threat Reduction Agency (DTRA) Grant No. HDTRA1-08-1-0036 and was completed with support from the Office of Naval Research (ONR) Grant No. N000014-12-1-0555. Simulations were performed at the Center for High Performance Computing of the University of Southern California.

¹S. H. Fischer and M. C. Grubelich, in *24th International Pyrotechnics Seminar* (1998), pp. 231–286.

²S. F. Son, *Mater. Res. Soc. Symp. Proc.* **800**, 161–172 (2004).

³H. C. Wu, H. J. Ou, H. C. Hsiao, and T. S. Shih, *Aerosol Air Qual. Res.* **10**(1), 38–42 (2010).

⁴B. S. Bockmon, M. L. Pantoya, S. F. Son, B. W. Asay, and J. T. Mang, *J. Appl. Phys.* **98**(6), 064903 (2005).

⁵S. A. Rashkovskii, *Combust. Explos. Shock Waves* **43**(6), 654–663 (2007).

⁶A. P. Il'in, E. M. Popenko, A. A. Gromov, Y. Y. Shamina, and D. V. Tikhonov, *Combust. Explos. Shock Waves* **38**(6), 665–669 (2002).

⁷V. G. Grigorev, V. E. Zarko, and K. P. Kutsenogii, *Combust. Explos. Shock Waves* **17**(3), 245–251 (1981).

⁸V. V. Karasev, A. A. Onischuk, O. G. Glotov, A. M. Baklanov, A. G. Maryasov, V. E. Zarko, V. N. Panfilov, A. I. Levykin, and K. K. Sabelfeld, *Combust. Flame* **138**(1–2), 40–54 (2004).

⁹E. W. Price, R. K. Sigman, J. K. Sambamurthi, and C. J. Park, Technical Report No. A118128, Georgia Institute of Technology, 1982.

¹⁰J. C. Mullen and M. Q. Brewster, *J. Propul. Power* **27**(3), 650–661 (2011).

¹¹J. Y. Malchi, R. A. Yetter, S. F. Son, and G. A. Risha, *Proc. Combust. Inst.* **31**, 2617–2624 (2007).

¹²M. Marion, C. Chauveau, and I. Gokalp, *Combust. Sci. Technol.* **115**(4–6), 369 (1996).

¹³A. Pivkina, P. Ulyanova, Y. Frolov, S. Zavyalov, and J. Schoonman, *Propellants, Explos., Pyrotech.* **29**(1), 39–48 (2004).

¹⁴M. R. Weismiller, J. Y. Malchi, J. G. Lee, R. A. Yetter, and T. J. Foley, *Proc. Combust. Inst.* **33**, 1989–1996 (2011).

¹⁵A. Bezmelnitsyn, R. Thiruvengadathan, S. Barizuddin, D. Tappmeyer, S. Apperson, K. Gangopadhyay, S. Gangopadhyay, P. Redner, M. Donadio, D. Kapoor, and S. Nicolich, *Propellants, Explos., Pyrotech.* **35**(4), 384–394 (2010).

- ¹⁶A. Prakash, A. V. McCormick, and M. R. Zachariah, *Chem. Mater.* **16**(8), 1466–1471 (2004).
- ¹⁷R. Shende, S. Subramanian, S. Hasan, S. Apperson, R. Thiruvengadathan, K. Gangopadhyay, S. Gangopadhyay, P. Redner, D. Kapoor, S. Nicolich, and W. Balas, *Propellants, Explos., Pyrotech.* **33**(2), 122–130 (2008).
- ¹⁸S. Subramanian, S. Hasan, S. Bhattacharya, Y. Gao, S. Apperson, M. Hossain, R. V. Shende, S. Gangopadhyay, P. Redner, D. Kapoor, and S. Nicolich, *Mater. Res. Soc. Symp. Proc.* **896**, 9–14 (2006).
- ¹⁹E. Perre, L. Nyholm, T. Gustafsson, P. L. Taberna, P. Simon, and K. Edstrom, *Electrochem. Commun.* **10**(10), 1467–1470 (2008).
- ²⁰Y. T. Pang, G. W. Meng, L. D. Zhang, W. J. Shan, C. Zhang, X. Y. Gao, and A. W. Zhao, *Solid State Sci.* **5**(7), 1063–1067 (2003).
- ²¹M. B. Pomfret, D. J. Brown, A. Epshteyn, A. P. Purdy, and J. C. Owrutsky, *Chem. Mater.* **20**(19), 5945–5947 (2008).
- ²²C. S. Li, W. Q. Ji, J. Chen, and Z. L. Tao, *Chem. Mater.* **19**(24), 5812–5814 (2007).
- ²³M. Saka and R. Nakanishi, *Mater. Lett.* **60**(17–18), 2129–2131 (2006).
- ²⁴Y. B. Lu, H. Tohmyoh, M. Saka, and H. L. Pan, *Optoelectron. Adv. Mater.* **5**(11), 1219–1222 (2011).
- ²⁵C. Langhammer, M. Schwind, B. Kasemo, and I. Zoric, *Nano Lett.* **8**(5), 1461–1471 (2008).
- ²⁶See supplementary material at <http://dx.doi.org/10.1063/1.4913490> for simulation details.
- ²⁷C. L. Yeh and K. K. Kuo, *Prog. Energ. Combust.* **22**(6), 511–541 (1996).
- ²⁸M. Baram, D. Chatain, and W. D. Kaplan, *Science* **332**(6026), 206–209 (2011).
- ²⁹K. Shimamura, F. Shimojo, R. K. Kalia, A. Nakano, and P. Vashishta, *Phys. Rev. Lett.* **111**(6), 066103 (2013).
- ³⁰S. H. Oh, M. F. Chisholm, Y. Kauffmann, W. D. Kaplan, W. D. Luo, M. Ruhle, and C. Scheu, *Science* **330**(6003), 489–493 (2010).
- ³¹V. Laurent, D. Chatain, C. Chatillon, and N. Eustathopoulos, *Acta Metall. Mater.* **36**(7), 1797–1803 (1988).